Tethered multifluorophore motion reveals equilibrium transition kinetics of single DNA double helices

Matthias Schickinger[a], Martin Zacharias[b], and Hendrik Dietz[a,c,1]

[a]Laboratory for Biomolecular Design, Physics Department, Technische Universität München, 85748 Garching, Germany; [b]Lehrstuhl für Biomolekulare Dynamik, Physics Department, Technische Universität München, 85748 Garching, Germany; and [c]Institute for Advanced Study, Technische Universität München, 85748 Garching, Germany

Edited by Alan R. Fersht, Gonville and Caius College, Cambridge, United Kingdom, and approved June 26, 2018 (received for review January 12, 2018)

We describe a tethered multifluorophore motion assay based on DNA origami for revealing bimolecular reaction kinetics on the single-molecule level. Molecular binding partners may be placed at user-defined positions and in user-defined stoichiometry; and binding states are read out by tracking the motion of quickly diffusing fluorescent reporter units. Multiple dyes per reporter unit enable singe-particle observation for more than 1 hour. We applied the system to study in equilibrium reversible hybridization and dissociation of complementary DNA single strands as a function of tether length, cation concentration, and sequence. We observed up to hundreds of hybridization and dissociation events per single reactant pair and could produce cumulative statistics with tens of thousands of binding and unbinding events. Because the binding partners per particle do not exchange, we could also detect subtle heterogeneity from molecule to molecule, which enabled separating data reflecting the actual target strand pair binding kinetics from falsifying influences stemming from chemically truncated oligonucleotides. Our data reflected that mainly DNA strand hybridization, but not strand dissociation, is affected by cation concentration, in agreement with previous results from different assays. We studied 8-bp-long DNA duplexes with virtually identical thermodynamic stability, but different sequences, and observed strongly differing hybridization kinetics. Complementary full-atom molecular-dynamics simulations indicated two opposing sequence-dependent phenomena: helical templating in purine-rich single strands and secondary structures. These two effects can increase or decrease, respectively, the fraction of strand collisions leading to successful nucleation events for duplex formation.

single molecule | DNA | DNA nanotechnology | kinetics | hybridization

To acquire quantitative data about the kinetics of forming and breaking biomolecular interactions from an ensemble, it is necessary to push the system under study from one condition to another and then measure the rate of relaxation to equilibrium. The relaxation of an ensemble is governed by a superposition of the elementary reaction processes in the system. By contrast, on the level of single molecules, elementary molecular transitions may be observed directly in equilibrium. Consequently, molecular heterogeneity and how external factors influence elementary processes can be revealed in single-molecule measurements. However, studying reversible interactions between two separate biomolecules in solution on the single-molecule level requires means for preventing the exchange of these molecules with others from solution.

One attractive approach that can circumvent molecular exchange relies on tracking tethered particle or tethered fluorophore motions (TPM or TFM, respectively). It has been used previously in many single-molecule studies on, for example, the kinetics of transcription (1–3), DNA looping (4–21), DNA mechanics (22–24), recombination (25–31), nuclease activity (32), and DNA–DNA or protein–DNA binding (33–35). In these assays, one end of a molecular tether is fixed to a surface, while the other end is fixed to a probe such as a microsphere or a fluorophore whose position may be tracked in a microscope to discriminate different states in the system. The states of the system typically manifest in a different extent of diffusive displacements of the probe. Based on the prior work, it is easy to imagine a TPM assay that enables observing repeated unbinding and rebinding of user-defined interacting molecules fixed to either end of a tether. Such an assay would enable making binding state observations in parallel for many pairs of molecules, where each tethered reactant pair may be considered as a 100% pure sample. The system would be particularly attractive in the presence of molecular heterogeneity that could affect the reaction kinetics. For protein–protein or protein–nucleic acid binding, molecular heterogeneity could arise from posttranslational modifications such as glycosylation or phosphorylation, or from epigenetic markers such as DNA methylation. For DNA hybridization, chemically defective strands with truncations or base omissions in oligonucleotides are likely to exhibit different hybridization and dissociation kinetics. Revealing such kinetic heterogeneity is virtually impossible in ensemble measurements and poses a difficult challenge for single-molecule measurements in which binding partners can exchange, but a TPM assay should be capable to deal with it.

To realize bimolecular measurements with a TPM assay, several challenges need to be addressed: (*i*) fixing the molecular binding partners to either end of the tether in the desired stoichiometry, (*ii*) ensuring the mutual accessibility of the reaction partners, (*iii*) minimizing the influence of the probe on tether dynamics, and (*iv*) enabling long-term observations and precision tracking (6, 36). Here, we took advantage of advances in DNA

Significance

Understanding cellular functions and dysfunctions often begins with quantifying the interactions between the binding partners involved in the processes. Learning about the kinetics of the interactions is of particular importance to understand the dynamics of cellular processes. We created a tethered multifluorophore motion assay using DNA origami that enables over 1-hour-long recordings of the statistical binding and unbinding of single pairs of biomolecules directly in equilibrium. The experimental concept is simple and the data interpretation is very direct, which makes the system easy to use for a wide variety of researchers. Due to the modularity and addressability of the DNA origami-based assay, our system may be readily adapted to study various other molecular interactions.

Author contributions: H.D. designed research; M.S. performed research; M.Z. designed and performed MD simulations; M.S. analyzed experimental data; and M.S., M.Z., and H.D. wrote the paper.

The authors declare no conflict of interest.

This article is a PNAS Direct Submission.

[1]To whom correspondence should be addressed. Email: dietz@tum.de.

This article contains supporting information online at www.pnas.org/lookup/suppl/doi:10.1073/pnas.1800585115/-/DCSupplemental.

Published online July 23, 2018.

nanotechnology (37–39) and established a tethered particle assay for revealing bimolecular reaction kinetics that addresses successfully all of the above-mentioned issues.

Our current understanding of the kinetics of DNA hybridization mainly stems from studies of ensemble relaxation dynamics upon temperature changes, shock waves, or concentration jumps (40–49). Previous single-molecule fluorescence measurements have enabled directly observing hybridization and dissociation reactions in equilibrium (50–53) and have yielded more direct insight into how external conditions influence the underlying processes. Experimental data shedding light on how sequence controls the elementary reaction directions of double-helical DNA domain formation and dissociation are still scarce (49, 54), but such data may help making more informed decisions in the design of DNA-based biosensors, dynamic DNA nanodevices, and DNA computing circuits. It may also contribute to understanding the dynamics of DNA double helices in cellular contexts. We thus applied our assay to acquire quantitative data for DNA hybridization and dissociation reaction kinetics. We obtained these data through direct single-molecule observations of repeated binding and unbinding transitions of DNA single-strand pairs in unperturbed, true equilibrium.

To obtain qualitative insights into the molecular origins of our experimental results, we complemented them with all-atom molecular-dynamics (MD) simulations. A variety of simulation models with varying resolutions and parameters has been previously developed that allow studying reversible DNA hybridization and dissociation (55–57). Except for atomistic MD simulation studies of base pair opening and closing (fraying) at double-strand termini (58), the process of DNA hybridization has so far been studied by simulations employing a coarse-grained (CG) representation of the DNA partner molecules (54–57, 59, 60). CG models have been used to study the thermodynamics of different DNA sequences (59) and the kinetics of hybridization for long uniform sequences (55). However, CG models are parameterized to form dsDNA as a global optimum on a very smooth energy landscape and reproducing experimental stability. During the process of double-strand formation, DNA partners can form numerous non-Watson–Crick type hydrogen-bonding contacts and noncanonical intermediate motifs, which may not be well represented in a CG model without detailed atomistic interactions such as hydrogen bonds. We thus present here all-atom MD simulations in implicit solvent of reversible hybridization and dissociation of DNA duplexes.

Results

Establishing a Tethered Multifluorophore Motion Assay. We used standard multilayer DNA origami design methods (38, 61–63) and constructed two fluorescently labeled reporter units with radius of gyration on the scale of 15 nm to construct our upgraded TPM assay (Fig. 1*A*). To ensure high brightness and to prolong the observation time in single-particle fluorescence microscopy, we attached 20 copies of the organic dyes cyanine-3 and cyanine-5 onto each reporter unit, respectively (Fig. 1 *B* and *C*). The reporter units serve the purpose of anchoring the fluorescent dyes onto a structurally well-defined particle while maintaining a minimum interdye distance to suppress quenching. Furthermore, one of the two reporter units was functionalized

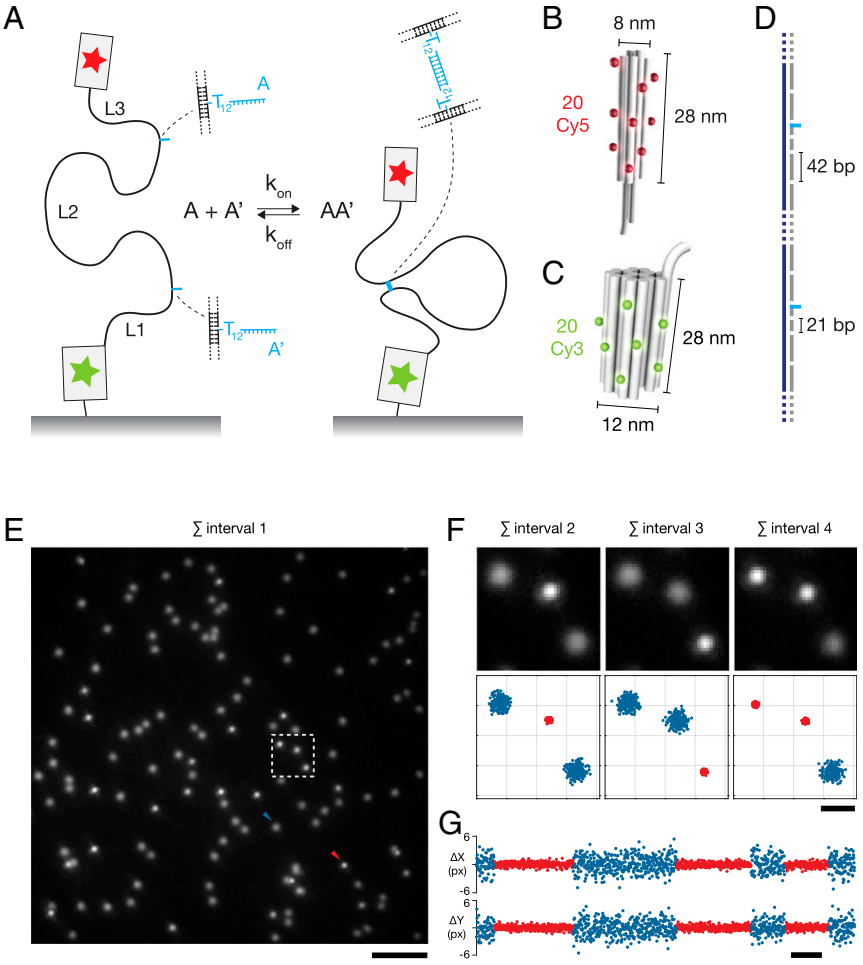

Fig. 1. Tethered multifluorophore motion assay based on DNA origami. (*A*) Schematic illustration of the tethered multifluorophore motion setup. Green star: Immobile reporter unit, fixed to a PEGylated microscope cover glass via up to six biotin–NeutrAvidin bonds. Red star: Mobile reporter unit, connected via a nicked double-helical tether with user-defined length to the immobile unit. On the tether, molecular targets may be presented. Here, DNA single strands with complementary sequence motifs. (*B* and *C*) Schematic representations of the reporter units built with multilayer DNA origami. Cylinders: DNA double helices. Red and green spheres represent fluorescent labels Cy5 and Cy3 attached to the solvent-exposed ends of 20 staples in the mobile and in the immobilized unit, respectively. Measures in nanometers are the height and the longest distance along the cross-section perpendicular to the helix axes. (*D*) Illustration of the nicked double-stranded tether. Dark blue: Scaffold strand; gray: staple oligonucleotides; light blue: 3′-ends of staples that carry the reaction partners A and A′. (*E*) Representative field of view in a TIRFM experiment, Cy5 spectral channel, averaged over a 10-s interval. Arrows indicate exemplary particles dwelling in the unbound, diffusive (blue) and bound, localized state (red) within that interval. (Scale bar, 5 μm.) Dashed box marks the region of interest depicted in *F*. (*F*, *Top* row) Close-ups on three Cy5-labeled reporter units over the course of three different 20-s time intervals. (*F*, *Bottom* row) Scatter plots of the positions obtained by centroid tracking during the same intervals. Note the changes in appearance of the average images and the *XY* spread of the particles' positions. (Scale bar, 1 μm.) (*G*) Exemplary cutout from a single-particle *XY* trajectory featuring alternating dwells in the high-mobility (blue) and low-mobility (red) states. (Scale bar, 10 s.)

for stable immobilization of this unit on microscope glass slides with up to six biotin–NeutrAvidin connections (see *SI Appendix*, Figs. S1–S4 for details of the reporter unit design). We connected the two reporter units using a double-stranded DNA tether having single-strand nicks every 42 bp. This design allows attaching molecules at specific sites within the tether by exchanging particular oligonucleotides with their appropriately modified counterparts (Fig. 1*D*).

In the work presented here, two DNA single strands branch off from the tether at distances of L1 and L3 bp, respectively, counting from each reporter unit, which leaves a tether segment of length L2 base pairs between the two single strands. In addition to polythymine stretches that promote accessibility and orientation randomization, the two DNA single strands contained the complementary sequence motifs A and A′. The two single strands may thus form a double-helical DNA domain whose hybridization and dissociation is coupled to looping and unlooping, respectively, of the segment L2. In the bound state, the two fluorescent reporter units are separated with a short tether L1 + L3 base pairs long, while in the dissociated state of the bimolecular reaction under study the tether lengthens to L1 + L2 + L3, thereby extending the range of diffusive motion of the mobile reporter unit. We tested two geometries for anchoring the DNA single-strand targets within the tether system: proximal attachment, where both targets are anchored in close vicinity of the reporter units (L1 = 0 bp; L3 ∼ 60 bp), and distal attachment of the target strands away from the reporter units, with L1 and L3 having ∼300 bp length.

Similar as in previously described tethered (single) fluorophore motion assays (6, 25), for adequately chosen L2, it is possible to detect the bound and unbound states of the molecular system under study by tracking the motion of individual mobile reporter units using a fluorescence microscope (Fig. 1*E* and Movie S1) and discriminating intervals of lower and higher mobility, respectively. Because of the tethering, reversible hybridization and dissociation of the same pair of DNA single strands may be observed (Fig. 1 *F* and *G*). We acquired data using stroboscopic illumination (6) with alternating laser excitation (64) in a total internal reflection fluorescence microscope (TIRFM). The data allowed determining with subdiffraction precision the position of the mobile reporter unit relative to the immobilized unit using centroid tracking (65, 66), independent of the binding state. The spot tracking leads to trajectories of *XY* displacement over time of the mobile reporter unit relative to its mean position (Fig. 1*G* and *SI Appendix*, Fig. S5). The up to 75-min-long time traces reveal the relevant conformational states per single particle. These states include the designed hybridized conformation with looped tethers, leading to periods with small position fluctuations, and the dissociated conformations that are characterized by larger displacements.

For the analysis, we classified the single-particle displacement–time traces using maximum-likelihood hidden-Markov modeling (HMM) (67–69), and then determined the dwell times of the individual particles in the hybridized and dissociated states. Photobleaching of the fluorophores leads to decreasing signal-to-noise ratio (SNR) over time, which affects the particle tracking accuracy. The effect was included in our hidden-Markov treatment. For details, see *SI Appendix*, *Materials and Methods* and Figs. S6–S8. The prolonged illumination could potentially also damage the reporter units, the tether, or the reactant pair. However, the distributions of lifetimes that we obtained from consecutive intervals of 15-min length match closely (*SI Appendix*, Fig. S9). The lack of a time-dependent effect on the lifetimes indicates the absence of photoinduced alteration of sample behavior. Occasionally, we observed off-target binding to sticky patches on the microscope slides (*SI Appendix*, Fig. S10), which we also accounted for.

Tethered Multifluorophore Motion Resolves Molecular Heterogeneity. In our assay, molecular heterogeneity in a sample may be discovered by acquiring many single-particle recordings, extracting particle displacement–time traces, and determining the average dwell times in unbound and bound states for each particle. For DNA oligonucleotides prepared by chemical synthesis as we studied them in this work, we may expect molecular heterogeneity stemming for example from chemical truncations. Preparing a scatter plot of the determined mean bound vs. mean unbound dwell times reveals multiple data point clusters, as exemplified with data that we acquired with a sample featuring two strands A and A′ that can form an 8-bp-long double-helical DNA domain with sequence CCTCCTCC:GGAGGAGG (Fig. 2*A*). There is a main population of single-particle recordings that exhibited similar kinetic properties, but there were also particles that had substantially shorter bound-state lifetimes. Also, some particles took much longer on average to rebind but had similar bound-state lifetimes as the main population. Last, there were also a few particles that had both longer rebinding and shorter bound-state lifetime. Exemplary single-particle recordings from each of the scatter plot clusters clearly show that the respective particles exhibit quite distinct behavior, which must originate from molecular differences (Fig. 2*B*).

We attribute the population of particles with substantially shorter mean bound dwell times compared with the main population to particles having defective interaction sequences A and A′ stemming from truncated synthesis products. This interpretation is supported by data obtained from experiments with a 9-bp motif CCAGAGACG:CGTCTCTGG and an 8-bp motif CAGGAACG:CGTTCCTG in the proximal attachment geometry. Short bound-state dwell time outliers of the 9-bp variant behave similarly to the main population of the 8-bp variant (Fig. 2*C* and *SI Appendix*, Fig. S11). We attribute long unbound-state dwell time outliers to particles with defects in our reporter units that lead to reduced accessibility of the molecular binding partners, which is particularly relevant for the proximal attachment geometry.

To provide an objective criterion for classifying the individual particles into main population and outliers, we use a probability-thresholding approach. Each single-particle recording is characterized by N dwells in each of the two states (bound and unbound) with stochastically distributed durations. For the purpose of sorting particles, we assume that the individual dwells follow single-exponential probability density distribution with global rate parameters. The probability for observing a particular sum of N dwell times in each state based is then given by an Erlang distribution. A particle was declared an outlier if, in either of the two states, its sum of dwell times was within the far tails of the distribution (<2/1,000,000 probability; *Materials and Methods*). The fraction of particles that were discarded as outliers by this approach varied between a few percent and up to 30%, depending on the sample.

Analysis of histograms derived by pooling all recorded individual single-particle dwell times in bound and unbound states from particles sorted into the main population (Fig. 2*D*) reveals that the data from the main population obey nearly ideally single-exponential decays, which strongly argues for homogeneity. The shape of the histogram for particles declared as outliers cannot be explained by a single-exponential decay. Instead, it reflects a mixture of processes having different stochastic behavior. Simply pooling all data into one class, as it would be unavoidable in ensemble measurements (49) and difficult to avoid in single-molecule assays with binding-partner exchange (51–53, 70), can lead to substantial errors in the determination of the kinetic rates of the target process under study (Fig. 2*D*). For instance, in the case of the 9-bp double-helical DNA domain, including outliers into the statistics would result in underestimating the hybridization rate by about 30%, and overestimating the off-rate by about 45%.

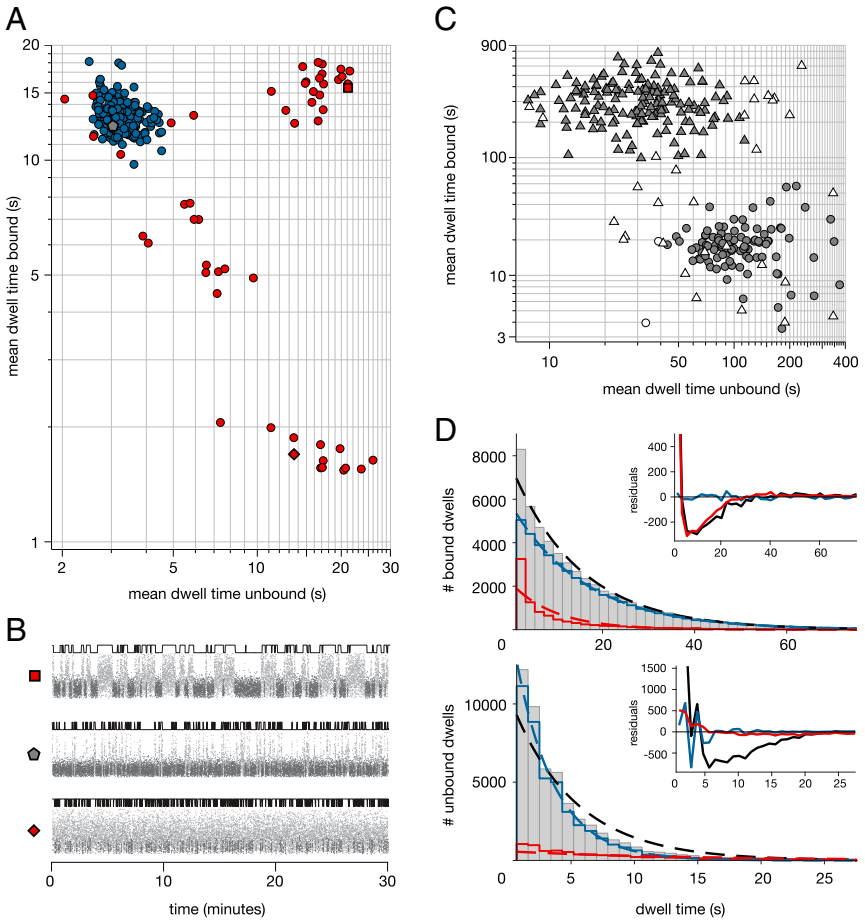

Fig. 2. Molecular heterogeneity in tethered multifluorophore motion measurements. (*A*) Mean bound vs. mean unbound dwell times per single-particle trajectory, 8-bp sequence motif CCTCCTCC:GGAGGAGG, 1,554-bp tether, distal attachment geometry, at 0.5 mol/L NaCl. Blue: Main population. Red: Discarded particles (see *Materials and Methods* for details). (*B*) Representative traces of radial displacement over time. Dark small markers: Dwells of low mobility. Light small markers: High-mobility dwells. Black line: State trajectory from HMM analysis, indicating bound (lower level) and unbound state (upper level). Top and bottom trace: Discarded single particles. Middle trace: Particle within the main population cluster. Large markers as in *A*. (*C*) Mean bound vs. mean unbound dwell times per single-particle trajectory, 1,554-bp tether, proximal attachment geometry, at 0.5 mol/L NaCl. Triangles: 9-mer motif CCAGAGACG:CGTCTCTGG. Circles: 8-mer motif CAGGAACG:CGTTCCTG. Filled markers: Main population. Empty markers: Outliers. (*D*) Histograms of dwell times in bound (*Top*) and unbound states (*Bottom*). Gray bars: All particles. Solid blue line: Main population. Solid red line: Outliers. Blue, red, and black dashed lines: Single-exponential fits to main population, outliers, and all particles, respectively. (*Insets*) Residuals of histogram counts from fit.

Tether Length and Anchor Sites of Reactants Influence On-Rate, but Not Off-Rate. The length of the looping tether will directly affect the rate of duplex formation by influencing how frequently the two molecular targets will diffusively hit each other, similar to how the concentrations of reactants influence the rate at which molecules randomly collide. Regarding the bound states, it is conceivable that the forces that counteract looping could also cause accelerated unbinding of the duplex, similar to the way pulling on DNA duplexes in atomic force microscopy or optical tweezers can induce helix melting and strand dissociation (71). To quantify the effect of tether length on the binding kinetics, we studied exemplarily the reversible hybridization and dissociation of an 8-bp-long DNA duplex with sequence CAGGAACG:CGTTCCTG using three different tether lengths in the distal attachment geometry (Fig. 3) and using five tether lengths in the proximal attachment geometry (*SI Appendix*, Fig. S12). On the level of single-particle position time traces, it is readily apparent that increasing the tether length leads to an increased duration of the heavily fluctuating, unbound states (Fig. 3 *A*–*C*). We collected many single-particle displacement–time traces from fluorescence movies, separated outliers from the main species as described above, and computed the average time each analyzed particle spent in bound vs. unbound states. The scatter plots shown in Fig. 3*D* show these data pooled from hundreds of particles and reflect slower rebinding kinetics for longer tether length. By contrast, the unbinding kinetics has negligible dependence on tether length.

We pooled the dwell times each single particle spent in unbound and bound states and computed lifetime histograms. The resulting distributions containing thousands of single-duplex hybridization and dissociation events from several hundred independent single-particle recordings are virtually indistinguishable from single-exponential decays (Fig. 3*E*). Therefore, our tethered particle system realizes a two-state system that is described by two characteristic transition rate constants. Possible intermediates such as partially hybridized states either do not occur or have lifetimes below our detection limit. The observed behavior is consistent with the nucleation-zippering model of DNA hybridization (72). The dependence of the on-rate (inverse of the mean dwell time particles spent in the unbound states) on tether length (Fig. 3*F*, *Left*) may be explained with a simplified model of the entropic and enthalpic looping penalties according to $k_{on} \sim (N^{-3/2} \cdot e^{-A/N})$, where N is tether length in base pairs and A is a constant (see *Materials and Methods* for details). The model resembles the previously reported j-factor dependence of DNA duplex length (73). The average off-rate was ∼0.05 s^{-1} independent of tether length (Fig. 3*F*, *Right*).

We found that the distal attachment geometry yielded faster rebinding kinetics compared with proximal attachment of the two target strands (*SI Appendix*, Fig. S12). Presumably, placing the two targets at some distance from the reporter units alleviates steric exclusion effects and reduces constraints regarding the relative orientation for productive binding events. The distal geometry is then more similar to unrestricted binding events in solution. *SI Appendix*, Table S1 provides a summary of all experimentally determined rates, as well as the sizes of the corresponding datasets.

Concentration of Monovalent Salt Affects On-Rate, but Not Off-Rate. We carried out measurements on equilibrium duplex hybridization and dissociation as a function of salt concentration from physiological 0.15 mol/L up to 1 mol/L sodium chloride. We performed three sets of experiments with three different tether

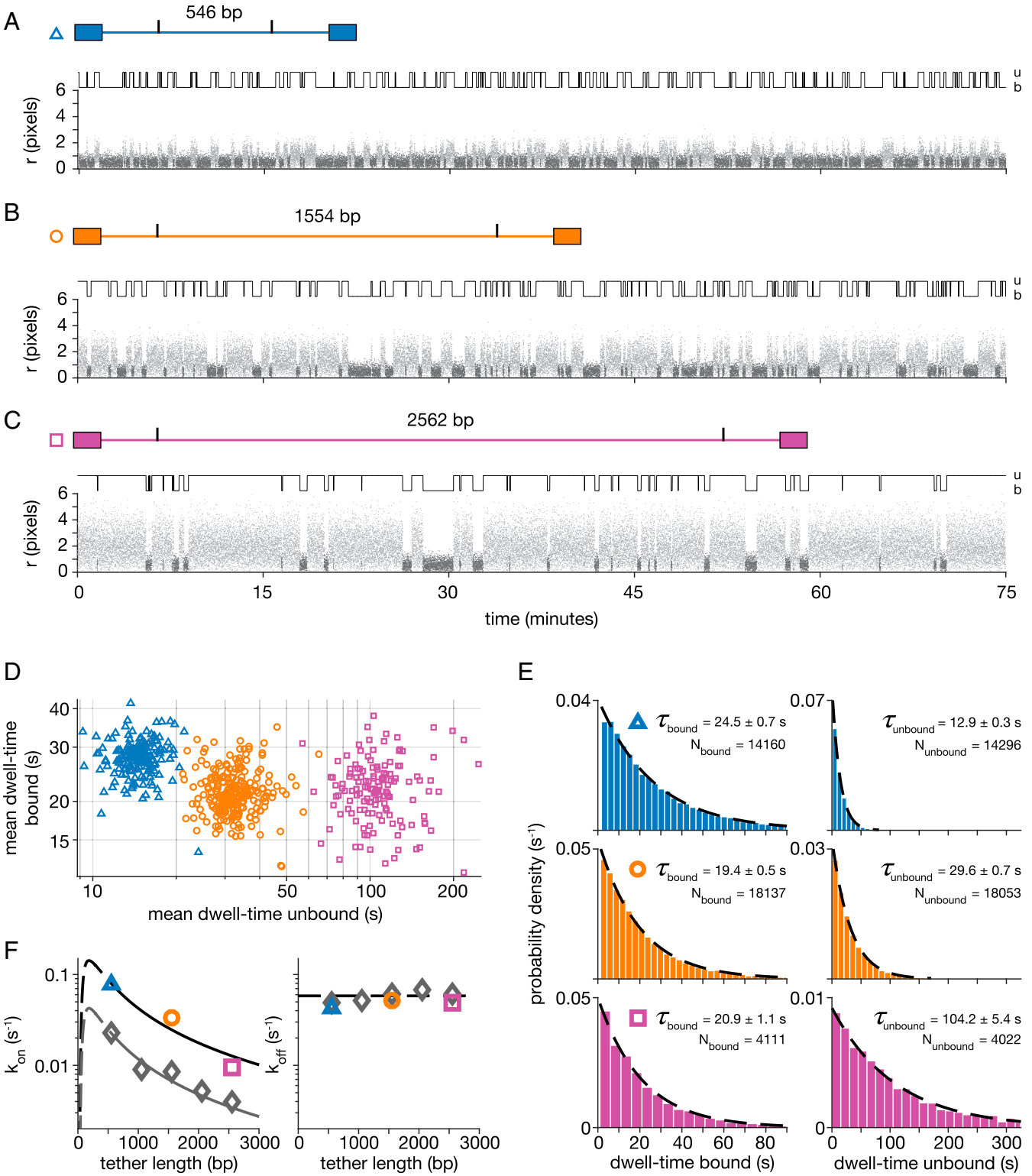

Fig. 3. Kinetics of duplex formation and dissociation for three different tether lengths. (*A*) Typical particle trajectory of $r = \sqrt{\Delta x^2 + \Delta y^2}$ over time. Duplex CAGGAACG:CGTTCCTG, 546-bp tether, distal attachment geometry, at 0.5 mol/L NaCl. Dark markers: Dwells of low mobility. Light markers: High-mobility dwells. Black line: State trajectory from HMM analysis, indicating bound (lower level) and unbound state (upper level). *B* and *C* as in *A*, but 1,554-bp and 2,562-bp tethers, respectively. (*D*) Mean bound vs. mean unbound dwell times per single-particle trajectory. Blue triangles: 546-bp tether. Orange circles: 1,554-bp tether. Purple squares: 2,562-bp tether. (*E*) Probability density histograms for dwell-times in the bound (*Left* column) and unbound state (*Right* column). *Top* to *Bottom*: 546-bp tether (blue), 1,554-bp tether (orange), and 2,562-bp tether (purple). Dashed lines: Truncated single-exponential probability densities from maximum-likelihood estimates. τ's: Inverse of the determined rate parameters. Errors: Statistical error from bootstrapping procedure ($\pm 3\sigma$). *N*'s: Total numbers of dwell times pooled for the corresponding state and tether length. (*F*) On-rate (*Left*) and off-rate (*Right*) vs. tether length. Blue, orange, and purple markers as in *D*. Gray markers: Data from 546-, 1,050-, 1,554-, 2,058-, and 2,562-bp tethers, proximal attachment geometry. Lines: Least-squares fits of the simplified model for influence of looping penalties on on-rate (*Materials and Methods*) to the data (*Left*), or mean value of all off-rates (*Right*).

lengths and using exemplarily an 8-bp-long DNA duplex with sequence CAGGAACG:CGTTCCTG (Fig. 4 *A*–*C*). We do not observe a systematic effect of the concentration of sodium chloride on the rate of dissociation (Fig. 4*D*), beyond some slight variation in the measured dissociation rates. The factor between the fastest and slowest measured value was ∼1.4. The little differences we measure might be attributable to other external factors, such as slight temperature variations (on the order of 1 °C) in our experiment. By contrast, increasing the concentration of sodium chloride had a strong effect on the rate of hybridization, causing up to fivefold acceleration upon an increase from 0.15 to 1 mol/L (Fig. 4*E*).

The tether length-dependent curves for binding rates as a function of salt concentration are parallel when plotting the observed rates logarithmically (Fig. 4*E*). This behavior may be explained with an Arrhenius-like rate constant $k_{\mathrm{on}}(c,N) = A \cdot e^{-f(c)+g(N)/k_{\mathrm{B}}T}$, where the activation barrier height is a sum of two terms $f(c)$ and $g(N)$, with the former being a function of the salt concentration c and the latter term a function of the tether length N. Hence,

$$\ln(k_{\mathrm{on}}(c,N)) = \underbrace{\ln(A) + \frac{g(N)}{k_{\mathrm{B}}T}}_{\mathrm{offset}(N)} - \frac{f(c)}{k_{\mathrm{B}}T}.$$

The shape of our curves (Fig. 4*E*) is consistent with $f(c) \sim \ln(c)$. From the kinetic rates for hybridization and dissociation, one may compute the equilibrium constant $K_{\mathrm{eq}} = k_{\mathrm{on}}/k_{\mathrm{off}}$. Since k_{off} has negligible dependence on the salt concentration, while $\ln(k_{\mathrm{on}}) \sim \ln(c)$, within the margin of error our data are in agreement with the empirical linear relationship of $\ln(K_{\mathrm{eq}})$ vs. $\ln(c_{\mathrm{NaCl}})$ derived by SantaLucia and Hicks (74) from ensemble duplex melting experiments in solution.

Hybridization Kinetics Depend Strongly on Sequence. We applied our system to study how the hybridization and dissociation kinetics of double-helical DNA domains vary with sequence. We designed a set of seven test sequences having virtually identical duplex free energy, according to the two-state nearest-neighbor model of DNA thermodynamic stability (74). The sequences had varying propensities to form secondary-structure motifs in the single strands of each designed duplex. We computed p_{Hairpin}, the probability of at least one of the strands to reside in any secondary structure with stem length of at least two nucleotides, using free energies predicted by DINAmelt/mfold (75) (Fig. 5*A*). The expectation is that the existence of such competing secondary structures affects the binding kinetics as seen in previous ensemble measurements (47, 49, 76). We performed a tethered-particle assay for each sequence variant, using the same tether length of 1,554 bp for all variants, in the presence of 0.5 mol/L NaCl. We collected fluorescence videos, extracted position–time traces for hundreds of single particles per variant, and determined the average dwell times in unbound and bound states for each analyzed particle. The resulting data were pooled to give the scatter plot shown in Fig. 5*B*. As expected, the sequence variants have quite different hybridization and dissociation kinetics. Whereas the fastest hybridizing variant 1 rapidly binds on the scale of 3 s, the slowest variant spends on average ∼500 s in the unbound state. Also, the duplex dissociation kinetics varies significantly, albeit less strongly than the hybridization kinetics. The average duplex lifetimes ranged from ∼5 s to ∼30 s depending on the variant. The spread in the scatter plot per variant reflects on the one hand the sample SD, which is equal to the ensemble mean value for a single-exponential probability density, and on the other hand the spread also reflects the number of transitions recorded per single particle (Fig. 5*B*, *Insets*). In particular, variant 7, which displayed extremely slow rebinding kinetics, underwent only a few transitions per recorded single-particle time trace. Hence, in this case, the average dwell times determined from a single-particle trace are statistically less well-defined compared with the other variants, causing the greater data point scatter for variant 7. As in our previous experiments with different tether lengths, the distribution of dwell times for the hybridized (Fig. 5*C*) and dissociated states (Fig. 5*D*), which we

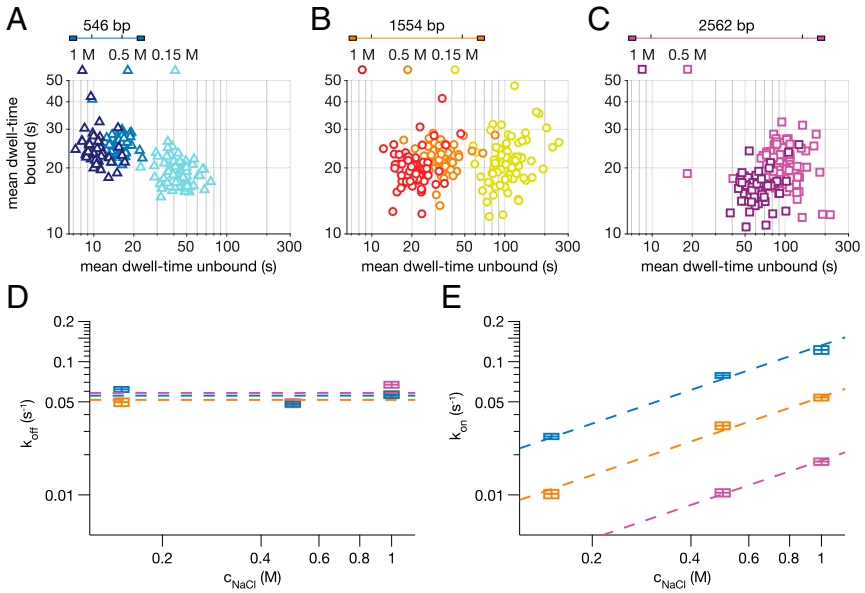

Fig. 4. The concentration of NaCl affects mainly the on-rate of duplex formation. (*A*) Mean bound vs. mean unbound dwell times per single-particle trajectory at different concentrations of NaCl, as indicated by shade of markers. Duplex CAGGAACG:CGTTCCTG, 546-bp tether, distal attachment geometry. *B* and *C* as in *A*, but 1,554- and 2,562-bp tethers, respectively. (*D*) Off-rate vs. concentration of NaCl. Blue markers: 546-bp tether, orange markers: 1,554-bp tether, purple markers: 2,562-bp tether. Marker width: ±5% error in salt concentration due to pipetting errors and possible evaporation. Marker height: Statistical error from bootstrapping procedure (±3σ). Dashed lines: Mean value of the off-rates measured for the corresponding tether length. (*E*) As in *D*, but on-rates. Dashed lines: Linear fits to the values of $\ln(k_{\mathrm{on}})$ vs. $\ln(c_{\mathrm{NaCl}})$.

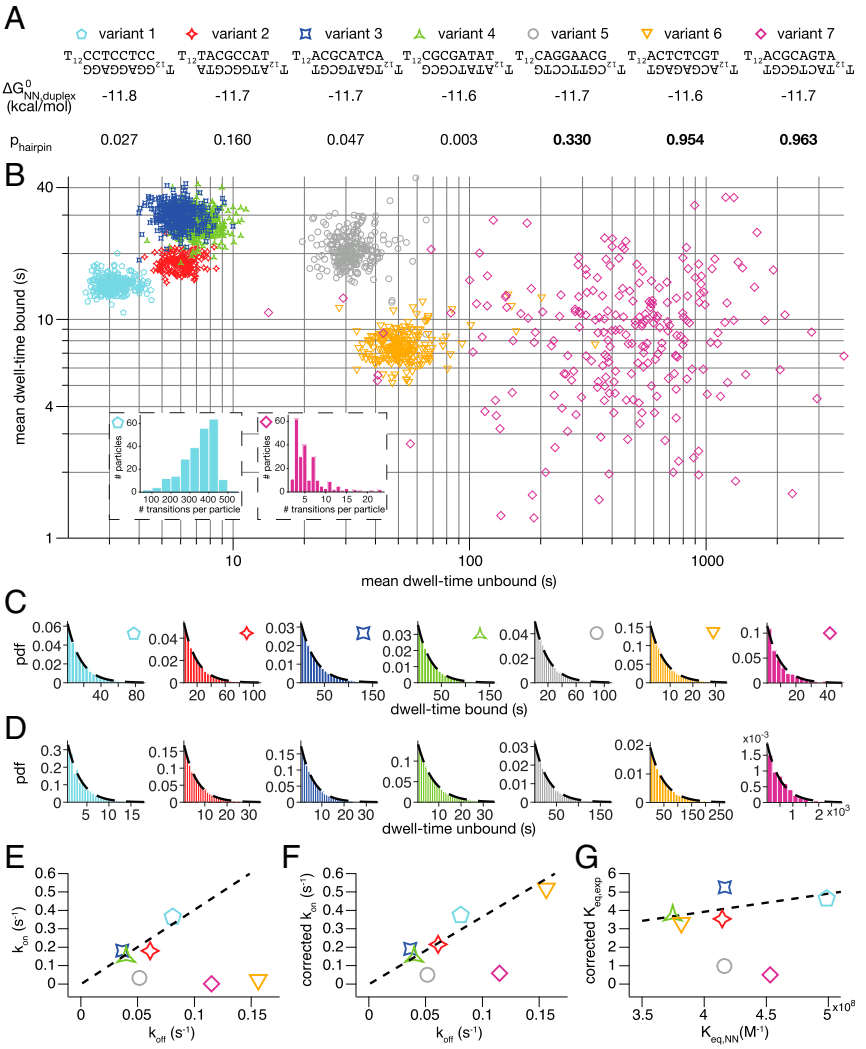

Fig. 5. The transition kinetics of short double-helical DNA domains strongly depends on sequence. (*A*) Seven iso-energetic duplex variants that we probed with our system. Every single-strand involved consists of a 12-thymine-long spacer and an 8-bp-long motif that is unique to that version and is reverse complementary to the corresponding opposite strand. The variants have very similar predicted values for the standard free energy of hybridization at T = 296.15 K, but differ in GC content, positioning of GC or AT pairs in terminal or central regions of the duplex, repetitiveness of sequence, and propensity to form hairpins. Energies of the duplexes and possible hairpin structures were computed with DINAmelt (75). p_{Hairpin} is the estimated equilibrium probability for any hairpins involving at least two nucleotides within an 8-bp motif to occur (*Materials and Methods*). (*B*) Mean bound vs. mean unbound dwell times per single-particle trajectory. 1,554-bp tether, distal attachment geometry, at 0.5 mol/L NaCl. Marker colors and shapes designate sequence variants as in *A*. (*Insets*) Histograms of the total number of state transitions per single-particle time trace for variants 1 and 7. (*C*) Probability density histograms for dwell times in the bound and (*D*) unbound state. Colors as in *A*. Dashed lines: Truncated single-exponential probability density functions from maximum-likelihood estimates (*Materials and Methods*). (*E*) Symbols: On-rate vs. off-rate. See *Materials and Methods* for details on calculation. Marker colors and shapes as in *A*. Dashed line: Least-squares fit to the data from variants 1–4. (*F*) As in *E*, but with on-rates corrected for secondary-structure propensity (measured on-rate divided by 1 − p_{Hairpin}). Dashed line: Least-squares fit to the data from variants 1–4 and 6. (*G*) Corrected equilibrium constant (corrected on-rate divided by off-rate) vs. nearest-neighbor prediction of K_{eq}. Dashed line: Fit to the data from variants 1–4 and 6 (slope: 9.84 × 10^{-9} mol/L).

obtained by pooling all single-particle transition dwell times per variant, were virtually indistinguishable from single-exponential decays, for all variants analyzed herein.

Since the free energy of binding for all tested duplex variants was designed to be nearly identical, the ratio of the hybridization rate over dissociation rate should be a constant if one were to assume that secondary structures within the single strands do not occur. The ratio then gives the equilibrium constant K_{eq}, or the negative natural logarithm of the free energy difference between the unlooped and looped states of the system under study. Indeed, when plotting the obtained hybridization rates over the dissociation rate, we see a linear relationship for the variants with low p_{Hairpin}, that is, variants 1–4. However, the ratios of the kinetic rates obtained for the sequence variants 5–7 with high p_{Hairpin} deviate significantly from the least-squares fit to the values from variants 1–4 (Fig. 5*E*).

As a first-order correction for the effect of secondary structures, we divided the measured on-rates by 1 − p_{Hairpin}, the calculated probability for both strands to reside in a conformation free from hairpins with stem length of two or more nucleotides. For our 8-bp-long duplex sequences, this approach is very similar to applying the model published by Hata et al. (76), with the assumption that Δ_{seq} = 1 for all nucleation sites. The correction yields an overall better agreement with a constant ratio of the kinetic rates (Fig. 5*F* and *SI Appendix*, Fig. S13), but variants 5 and 7 still deviate. Whereas there is only one possible hairpin structure in either strand of sequence variant 6, there are multiple possible secondary structures in the strands of variant 5 and

7, which presumably will interchange rapidly. A description that considers only discrete states as we do in our calculation of p_{Hairpin} may be overly simplified in such a case.

The K_{eq} that we determined are approximately linearly related to the equilibrium constants K_{eq}(NN) predicted by the nearest-neighbor model (Fig. 5*G*), as expected (*Materials and Methods*). The slope of the linear fit puts the effective reactant concentration in our tethered-particle system at ∼9.8 nM. Given our tether length of 1,554 bp, this value is consistent with previous effective concentration estimations (77).

Full-Atom MD Simulations of Reversible Hybridization and Dissociation. To help explain the molecular origin of the strong sequence dependence of the hybridization kinetics that we found experimentally, we used full-atom MD simulations, which were performed in a generalized Born-type implicit solvent (*Materials and Methods* and refs. 78 and 79). At 300 K, no reversible duplex formation could be observed during several microsecond simulation times. However, at elevated simulation temperatures (for the present simulation conditions: ∼340–350 K), it was possible to record multiple occurrences of reversible dissociation and rehybridization in single long-simulation trajectories (Fig. 6 *B–D* and Movie S2). When plotting the root-mean-square deviations (rmsd) of atom coordinates (heavy atoms) from the coordinates in standard B-DNA, time traces are obtained that reflect two-state like transitions, similar to the experimental data (Fig. 6 *B–D*). The simulations provide qualitative insight into the transition paths, as they reflect nucleation and subsequent fast propagation characterized by the initial formation of a short base pair contact and rapid zippering up to extend to the full duplex (Fig. 6 *E–H*). The propagation process occurs on a timescale of tens of nanoseconds after a successful initial nucleation, much faster than the time between successful encounters (Fig. 6 *E–H*). At the high simulation temperatures, no significant population of stable hairpin structures for the partner strands was observed. At lower simulation temperatures (e.g., 285 K, Fig. 6*I*) close to temperatures used in the experiments, the single-stranded partners of variants 6 and 7 sampled a high proportion of well-known GAGA tetraloop-like (80) and GCA triloop-like conformations (81) with one or two stem base pairs (Fig. 6*I* and Movie S3). Simulations of the single-stranded DNA partners indicate sequence-dependent tendencies of templating behavior: For example, in the case of sequence variant 1, which experimentally showed the highest hybridization rate, during the simulations the strand only containing purines frequently populates semihelical stacked conformations (Fig. 6 *J* and *K*). These offer a large exposed surface for initial binding of the partner strand, which raises the probability for forming a stable nucleus that promotes propagation rather than dissociation. Such tendency is also seen for fast-associating variant 2, and for variants 5 and 6. However, in the latter two cases, it is counteracted by the secondary structures in the dissociated single strands.

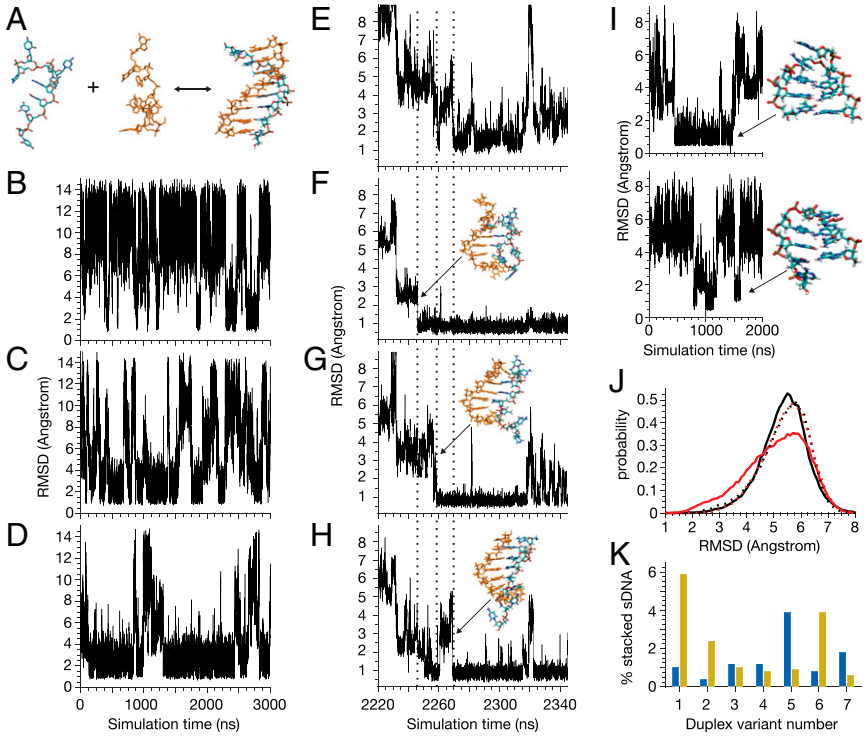

Fig. 6. Full-atom MD simulations. (*A*) Illustration of the reversible dsDNA formation and dissociation process for sequence variant 5 observed during MD simulations (stick model of DNA). (*B–D*) Root-mean-square deviation (rmsd) of heavy atoms (all nucleotides except terminal nucleotides) with respect to B-DNA vs. simulation time for simulations at 350 K (*B*), 345 K (*C*), and 340 K (*D*) (results shown for variant 5). An rmsd of <3 Å indicates double-strand formation except for possible fraying at the duplex termini. (*E–H*) Exemplary nucleation and propagation event of dsDNA formation: (*E*) rmsd vs. simulation time for the full duplex (variant 1). (*F*) Rmsd vs. simulation time of the fourth base pair step (a CC/GG dsDNA), (*G*) rmsd of the neighboring fifth base pair step (a CT/GA step) forming ∼10 ns after the first base pair step (indicated as vertical dotted lines). (*H*) Formation of the third base pair step. (*I*) Rmsd of sampled conformations with respect to hairpin reference structures (illustrated as stick models) from MD simulation of single strands at 285 K. (*I*, *Top*) Variant 6, strand ACGAGAGT, which forms a well-known GNRA-tetraloop. (*I*, *Bottom*) Variant 7, strand ACGCAGTA, forming a central GCA-triloop. Both hairpin structures include a characteristic sheared G:A loop-closing base pair. (*J*) Sequence-dependent tendency to form stacked single strands that adopt a structure close to B-form already in the absence of the partner strand, shown as probability distribution of rmsd with respect to a B-DNA reference, at elevated temperatures (2 μs at 345 K). Red/black solid lines: Fast-associating variant 1, strands GGAGGAGG and CCTCCTCC, respectively. Dotted lines: Both strands of variant 7. (*K*) Percentage of sampled stacked B-form–like single strands (in absence of binding partner) with rmsd relative to B-DNA < 3 Å. Blue/yellow bars represent the first/second strand.

Discussion

In addition to establishing our assay, we saw that the concentration of monovalent ions has little influence on the duplex dissociation rates in the range from physiological concentration to 1 mol/L of NaCl. Our observations are consistent with the trends observed in previous single-molecule equilibrium FRET measurements with a 9-bp-long duplex (50), carried out in a lower salt regime from 5 to 50 mM NaCl, and with data from single-molecule confocal FRET measurements, albeit the authors describe a somewhat differing twofold decrease in the dissociation rate upon increasing the NaCl concentration from 0.1 to 1 mol/L (51). Our findings are also consistent with previous ensemble laser spectroscopic (44) and NMR (45) kinetic relaxation measurements after thermal jumps, which indicated salt concentration predominantly affects the association rates. However, in previous single-molecule FRET measurements with intramolecular DNA hairpin opening and closing, both reaction directions were affected by the salt concentration (82, 83), which raises the question of what causes the different behavior in the intramolecular (hairpin) vs. intermolecular hybridization.

Complementary to our experimental hybridization studies, we found that it is also possible to follow reversible duplex formation and dissociation in silico on the microsecond timescale, if we employ an implicit generalized Born solvent model, a reduced solvent viscosity, and elevated simulation temperatures compared with the experimental conditions. While a quantitative comparison with the experiments is not possible, the simulations provide qualitative insights on the order of the initial association and propagation events. In agreement with the present experiments, the simulations predict an apparent two-state association process. This process consists of two subprocesses, an initial successful encounter followed by a rapid propagation that is much faster than the time between successful binding events. On the one hand, the simulations identify a "templating" effect of certain sequences to adopt transiently single-stranded stacked conformations, which facilitates strand association and duplex formation by enhancing the accessibility of binding positions with a few nucleotides length, and thus increasing the probability of forming productive encounter complexes between segments of both partners. It can also speed up the subsequent propagation process. On the other hand, the simulations showed that indeed stable hairpin structures of the single strands are formed in cases with experimentally observed reduced association kinetics. It agrees with previous experimental studies that also found a significant decrease of the hybridization kinetics due to secondary-structure formation in the single strands (47, 76). However, hairpin formation may also affect the melting process (57), which is supported by an observed increase in the off-rate for the two sequences (6 and 7) with highest hairpin propensities.

In summary, our tethered multifluorophore motion assay affords several attractive qualities. It enables long-term precision particle tracking in fluorescence, with about two orders of magnitudes longer observation times compared with single-fluorophore assays (6). The longer recordings expand the accessible window of transition lifetimes and allow collecting more transitions per particle, resulting in more reliable statistics. Molecular heterogeneity in the sample may be thus discovered and dealt with as we described. Due to the modularity and addressability of the DNA origami-based tethered particle assay, we also expect that it may be readily adapted to study reversible equilibrium binding kinetics of many other target systems beyond DNA duplexes. By taking advantage of molecular conjugation methods (84–87), protein–nucleic acid interactions, protein–protein interactions, and protein–ligand interactions could also be studied on the single-molecule level. For instance, to apply the assay to the study of a pair of interacting proteins, only two oligonucleotides need to be exchanged for the corresponding protein–DNA conjugates. For applications to protein–DNA interactions, one must consider that the tether may contain additional binding sites, which could interact with the protein under study. We expect that off-target binding with significant lifetime would manifest in the data as additional discrete states. Unwanted sequence motifs could be excluded a priori by modifying the scaffold strand. Similarly, users could also integrate multiple binding sites to perform comparative kinetic studies. In the future, it is also conceivable that multiple tethers and additional fluorescence dyes with different emission wavelengths may be integrated to study the sequence and kinetics of assembly of biomolecular complexes containing more than two reaction partners.

Materials and Methods

We used standard methods and chemicals for the design and preparation of our samples, which are described in *SI Appendix, Materials and Methods*. Instrumentation and procedures for data acquisition, as well as procedures and theoretical models for data analysis, are described in *SI Appendix, Materials and Methods*. The MD simulations are described in *SI Appendix, Materials and Methods*.

The authors declare that all data supporting the findings of this study are available within the paper, its supporting information files, or upon request from the authors.

ACKNOWLEDGMENTS. We thank Fabian Finger and Dominik Voglmaier for auxiliary experiments, and Jonas Funke, Christian Wachauf, Florian Praetorius, Thomas Gerling, and Fabian Kilchherr for discussions. This project was supported by European Research Council Starting Grant 256270, Deutsche Forschungsgemeinschaft through grants provided the Gottfried–Wilhelm–Leibniz Program and SFB863, and the ERASynBio project "BioOrigami," funded by Bundesministerium für Bildung und Forschung Grant 031 A 458.

1. Schafer DA, Gelles J, Sheetz MP, Landick R (1991) Transcription by single molecules of RNA polymerase observed by light microscopy. *Nature* 352:444–448.
2. Yin H, Landick R, Gelles J (1994) Tethered particle motion method for studying transcript elongation by a single RNA polymerase molecule. *Biophys J* 67:2468–2478.
3. Tolić-Nørrelykke SF, Engh AM, Landick R, Gelles J (2004) Diversity in the rates of transcript elongation by single RNA polymerase molecules. *J Biol Chem* 279: 3292–3299.
4. Finzi L, Gelles J (1995) Measurement of lactose repressor-mediated loop formation and breakdown in single DNA molecules. *Science* 267:378–380.
5. Beausang JF, et al. (2007) DNA looping kinetics analyzed using diffusive hidden Markov model. *Biophys J* 92:L64–L66.
6. May PFJ, et al. (2014) Tethered fluorophore motion: Studying large DNA conformational changes by single-fluorophore imaging. *Biophys J* 107:1205–1216.
7. Pouget N, Turlan C, Destainville N, Salomé L, Chandler M (2006) IS911 transpososome assembly as analysed by tethered particle motion. *Nucleic Acids Res* 34:4313–4323.
8. Vanzi F, Broggio C, Sacconi L, Pavone FS (2006) Lac repressor hinge flexibility and DNA looping: Single molecule kinetics by tethered particle motion. *Nucleic Acids Res* 34:3409–3420.
9. Lia G, et al. (2003) Supercoiling and denaturation in Gal repressor/heat unstable nucleoid protein (HU)-mediated DNA looping. *Proc Natl Acad Sci USA* 100:11373–11377.
10. Normanno D, Vanzi F, Pavone FS (2008) Single-molecule manipulation reveals supercoiling-dependent modulation of lac repressor-mediated DNA looping. *Nucleic Acids Res* 36:2505–2513.
11. Wong OK, Guthold M, Erie DA, Gelles J (2008) Interconvertible lac repressor-DNA loops revealed by single-molecule experiments. *PLoS Biol* 6:e232.
12. Han L, et al. (2009) Concentration and length dependence of DNA looping in transcriptional regulation. *PLoS One* 4:e5621.
13. Rutkauskas D, Zhan H, Matthews KS, Pavone FS, Vanzi F (2009) Tetramer opening in LacI-mediated DNA looping. *Proc Natl Acad Sci USA* 106:16627–16632.
14. Laurens N, et al. (2009) Dissecting protein-induced DNA looping dynamics in real time. *Nucleic Acids Res* 37:5454–5464.
15. Zurla C, et al. (2009) Direct demonstration and quantification of long-range DNA looping by the λ bacteriophage repressor. *Nucleic Acids Res* 37:2789–2795.
16. Laurens N, et al. (2012) DNA looping by FokI: The impact of twisting and bending rigidity on protein-induced looping dynamics. *Nucleic Acids Res* 40:4988–4997.
17. Rusling DA, Laurens N, Pernstich C, Wuite GJ, Halford SE (2012) DNA looping by FokI: The impact of synapse geometry on loop topology at varied site orientations. *Nucleic Acids Res* 40:4977–4987.
18. Manzo C, Zurla C, Dunlap DD, Finzi L (2012) The effect of nonspecific binding of lambda repressor on DNA looping dynamics. *Biophys J* 103:1753–1761.
19. Johnson S, Lindén M, Phillips R (2012) Sequence dependence of transcription factor-mediated DNA looping. *Nucleic Acids Res* 40:7728–7738.
20. Johnson S, van de Meent JW, Phillips R, Wiggins CH, Lindén M (2014) Multiple LacI-mediated loops revealed by Bayesian statistics and tethered particle motion. *Nucleic Acids Res* 42:10265–10277.

21. Revalee JD, Blab GA, Wilson HD, Kahn JD, Meiners JC (2014) Tethered particle motion reveals that LacI·DNA loops coexist with a competitor-resistant but apparently unlooped conformation. *Biophys J* 106:705–715.
22. Brinkers S, Dietrich HR, de Groote FH, Young IT, Rieger B (2009) The persistence length of double stranded DNA determined using dark field tethered particle motion. *J Chem Phys* 130:215105.
23. Kumar S, et al. (2014) Enhanced tethered-particle motion analysis reveals viscous effects. *Biophys J* 106:399–409.
24. Nelson PC, et al. (2006) Tethered particle motion as a diagnostic of DNA tether length. *J Phys Chem B* 110:17260–17267.
25. Pinkney JN, et al. (2012) Capturing reaction paths and intermediates in Cre-loxP recombination using single-molecule fluorescence. *Proc Natl Acad Sci USA* 109: 20871–20876.
26. Zawadzki P, et al. (2013) Conformational transitions during FtsK translocase activation of individual XerCD-dif recombination complexes. *Proc Natl Acad Sci USA* 110: 17302–17307.
27. May PFJ, Zawadzki P, Sherratt DJ, Kapanidis AN, Arciszewska LK (2015) Assembly, translocation, and activation of XerCD-dif recombination by FtsK translocase analyzed in real-time by FRET and two-color tethered fluorophore motion. *Proc Natl Acad Sci USA* 112:E5133–E5141.
28. Mumm JP, Landy A, Gelles J (2006) Viewing single lambda site-specific recombination events from start to finish. *EMBO J* 25:4586–4595.
29. Fan HF, Cox MM, Li HW (2011) Developing single-molecule TPM experiments for direct observation of successful RecA-mediated strand exchange reaction. *PLoS One* 6: e21359.
30. Fan HF (2012) Real-time single-molecule tethered particle motion experiments reveal the kinetics and mechanisms of Cre-mediated site-specific recombination. *Nucleic Acids Res* 40:6208–6222.
31. Fan HF, Ma CH, Jayaram M (2013) Real-time single-molecule tethered particle motion analysis reveals mechanistic similarities and contrasts of Flp site-specific recombinase with Cre and λ Int. *Nucleic Acids Res* 41:7031–7047.
32. Plénat T, Tardin C, Rousseau P, Salomé L (2012) High-throughput single-molecule analysis of DNA-protein interactions by tethered particle motion. *Nucleic Acids Res* 40:e89.
33. Dixit S, Singh-Zocchi M, Hanne J, Zocchi G (2005) Mechanics of binding of a single integration-host-factor protein to DNA. *Phys Rev Lett* 94:118101.
34. Zocchi G (2001) Force measurements on single molecular contacts through evanescent wave microscopy. *Biophys J* 81:2946–2953.
35. Guerra RF, Imperadori L, Mantovani R, Dunlap DD, Finzi L (2007) DNA compaction by the nuclear factor-Y. *Biophys J* 93:176–182.
36. Segall DE, Nelson PC, Phillips R (2006) Volume-exclusion effects in tethered-particle experiments: Bead size matters. *Phys Rev Lett* 96:088306.
37. Rothemund PW (2006) Folding DNA to create nanoscale shapes and patterns. *Nature* 440:297–302.
38. Douglas SM, et al. (2009) Self-assembly of DNA into nanoscale three-dimensional shapes. *Nature* 459:414–418.
39. Wagenbauer KF, et al. (2017) How we make DNA origami. *Chembiochem* 18: 1873–1885.
40. Wetmur JG, Davidson N (1968) Kinetics of renaturation of DNA. *J Mol Biol* 31: 349–370.
41. Craig ME, Crothers DM, Doty P (1971) Relaxation kinetics of dimer formation by self complementary oligonucleotides. *J Mol Biol* 62:383–401.
42. Porschke D, Uhlenbeck OC, Martin FH (1973) Thermodynamics and kinetics of helix-coil transition of oligomers containing Gc base pairs. *Biopolymers* 12:1313–1335.
43. Ikuta S, Takagi K, Wallace RB, Itakura K (1987) Dissociation kinetics of 19 base paired oligonucleotide-DNA duplexes containing different single mismatched base pairs. *Nucleic Acids Res* 15:797–811.
44. Williams AP, Longfellow CE, Freier SM, Kierzek R, Turner DH (1989) Laser temperature-jump, spectroscopic, and thermodynamic study of salt effects on duplex formation by dGCATGC. *Biochemistry* 28:4283–4291.
45. Braunlin WH, Bloomfield VA (1991) 1H NMR study of the base-pairing reactions of d(GGAATTCC): Salt effects on the equilibria and kinetics of strand association. *Biochemistry* 30:754–758.
46. Morrison LE, Stols LM (1993) Sensitive fluorescence-based thermodynamic and kinetic measurements of DNA hybridization in solution. *Biochemistry* 32:3095–3104.
47. Gao Y, Wolf LK, Georgiadis RM (2006) Secondary structure effects on DNA hybridization kinetics: A solution versus surface comparison. *Nucleic Acids Res* 34: 3370–3377.
48. Zhang DY, Winfree E (2009) Control of DNA strand displacement kinetics using toehold exchange. *J Am Chem Soc* 131:17303–17314.
49. Zhang JX, et al. (2017) Predicting DNA hybridization kinetics from sequence. *Nat Chem* 10:91–98.
50. Cisse II, Kim H, Ha T (2012) A rule of seven in Watson-Crick base-pairing of mismatched sequences. *Nat Struct Mol Biol* 19:623–627.
51. Dupuis NF, Holmstrom ED, Nesbitt DJ (2013) Single-molecule kinetics reveal cation-promoted DNA duplex formation through ordering of single-stranded helices. *Biophys J* 105:756–766.
52. Peterson EM, Manhart MW, Harris JM (2016) Single-molecule fluorescence imaging of interfacial DNA hybridization kinetics at selective capture surfaces. *Anal Chem* 88: 1345–1354.
53. Jungmann R, et al. (2010) Single-molecule kinetics and super-resolution microscopy by fluorescence imaging of transient binding on DNA origami. *Nano Lett* 10:4756–4761.
54. Ouldridge TE, Sulc P, Romano F, Doye JP, Louis AA (2013) DNA hybridization kinetics: Zippering, internal displacement and sequence dependence. *Nucleic Acids Res* 41: 8886–8895.
55. Hinckley DM, Lequieu JP, de Pablo JJ (2014) Coarse-grained modeling of DNA oligomer hybridization: Length, sequence, and salt effects. *J Chem Phys* 141:035102.
56. Ouldridge TE, Louis AA, Doye JP (2011) Structural, mechanical, and thermodynamic properties of a coarse-grained DNA model. *J Chem Phys* 134:085101.
57. Schreck JS, et al. (2015) DNA hairpins destabilize duplexes primarily by promoting melting rather than by inhibiting hybridization. *Nucleic Acids Res* 43:6181–6190.
58. Zgarbová M, Otyepka M, Šponer J, Lankaš F, Jurečka P (2014) Base pair fraying in molecular dynamics simulations of DNA and RNA. *J Chem Theory Comput* 10: 3177–3189.
59. Cragnolini T, Derreumaux P, Pasquali S (2013) Coarse-grained simulations of RNA and DNA duplexes. *J Phys Chem B* 117:8047–8060.
60. Šulc P, et al. (2012) Sequence-dependent thermodynamics of a coarse-grained DNA model. *J Chem Phys* 137:135101.
61. Douglas SM, et al. (2009) Rapid prototyping of 3D DNA-origami shapes with caDNAno. *Nucleic Acids Res* 37:5001–5006.
62. Castro CE, et al. (2011) A primer to scaffolded DNA origami. *Nat Methods* 8:221–229.
63. Ke Y, et al. (2009) Multilayer DNA origami packed on a square lattice. *J Am Chem Soc* 131:15903–15908.
64. Kapanidis AN, et al. (2005) Alternating-laser excitation of single molecules. *Acc Chem Res* 38:523–533.
65. Yildiz A, Tomishige M, Vale RD, Selvin PR (2004) Kinesin walks hand-over-hand. *Science* 303:676–678.
66. Berglund AJ, McMahon MD, McClelland JJ, Liddle JA (2008) Fast, bias-free algorithm for tracking single particles with variable size and shape. *Opt Express* 16:14064–14075.
67. Kruithof M, van Noort J (2009) Hidden Markov analysis of nucleosome unwrapping under force. *Biophys J* 96:3708–3715.
68. Stigler J, Rief M (2012) Hidden Markov analysis of trajectories in single-molecule experiments and the effects of missed events. *ChemPhysChem* 13:1079–1086.
69. Chodera JD, et al. (2015) Bayesian hidden Markov model analysis of single-molecule force spectroscopy: Characterizing kinetics under measurement uncertainty. arXiv: 1108.1430v1.
70. Peterson EM, Harris JM (2018) Identification of individual immobilized DNA molecules by their hybridization kinetics using single-molecule fluorescence imaging. *Anal Chem* 90:5007–5014.
71. Greenleaf WJ, Woodside MT, Block SM (2007) High-resolution, single-molecule measurements of biomolecular motion. *Annu Rev Biophys Biomol Struct* 36:171–190.
72. Pörschke D, Eigen M (1971) Co-operative non-enzymic base recognition. 3. Kinetics of the helix-coil transition of the oligoribouridylic–oligoriboadenylic acid system and of oligoriboadenylic acid alone at acidic pH. *J Mol Biol* 62:361–381.
73. Yan J, Kawamura R, Marko JF (2005) Statistics of loop formation along double helix DNAs. *Phys Rev E Stat Nonlin Soft Matter Phys* 71:061905, and erratum (2005) 72: 059901.
74. SantaLucia J, Jr, Hicks D (2004) The thermodynamics of DNA structural motifs. *Annu Rev Biophys Biomol Struct* 33:415–440.
75. Markham NR, Zuker M (2005) DINAMelt web server for nucleic acid melting prediction. *Nucleic Acids Res* 33(Suppl 2):W577–W581.
76. Hata H, Kitajima T, Suyama A (2017) Influence of thermodynamically unfavorable secondary structures on DNA hybridization kinetics. *Nucleic Acids Res* 46:782–791.
77. Yan J, Kawamura R, Marko JF (2005) Statistics of loop formation along double helix DNAs. *Phys Rev E Stat Nonlin Soft Matter Phys* 71:061905.
78. Mongan J, Simmerling C, McCammon JA, Case DA, Onufriev A (2007) Generalized Born model with a simple, robust molecular volume correction. *J Chem Theory Comput* 3:156–169.
79. Nguyen H, Pérez A, Bermeo S, Simmerling C (2015) Refinement of generalized Born implicit solvation parameters for nucleic acids and their complexes with proteins. *J Chem Theory Comput* 11:3714–3728.
80. Nakano M, Moody EM, Liang J, Bevilacqua PC (2002) Selection for thermodynamically stable DNA tetraloops using temperature gradient gel electrophoresis reveals four motifs: d(cGNNAg), d(cGNABg),d(cCNNGg), and d(gCNNGc). *Biochemistry* 41: 14281–14292.
81. Yoshizawa S, Kawai G, Watanabe K, Miura K, Hirao I (1997) GNA trinucleotide loop sequences producing extraordinarily stable DNA minihairpins. *Biochemistry* 36: 4761–4767.
82. Tsukanov R, Tomov TE, Berger Y, Liber M, Nir E (2013) Conformational dynamics of DNA hairpins at millisecond resolution obtained from analysis of single-molecule FRET histograms. *J Phys Chem B* 117:16105–16109.
83. Tsukanov R, et al. (2013) Detailed study of DNA hairpin dynamics using single-molecule fluorescence assisted by DNA origami. *J Phys Chem B* 117:11932–11942.
84. Trads JB, Tørring T, Gothelf KV (2017) Site-selective conjugation of native proteins with DNA. *Acc Chem Res* 50:1367–1374.
85. Lang K, Chin JW (2014) Cellular incorporation of unnatural amino acids and bioorthogonal labeling of proteins. *Chem Rev* 114:4764–4806.
86. Shaw A, Benson E, Högberg B (2015) Purification of functionalized DNA origami nanostructures. *ACS Nano* 9:4968–4975.
87. Jahn K, et al. (2011) Functional patterning of DNA origami by parallel enzymatic modification. *Bioconjug Chem* 22:819–823.

Correction

BIOPHYSICS AND COMPUTATIONAL BIOLOGY

Correction for "Tethered multifluorophore motion reveals equilibrium transition kinetics of single DNA double helices," by Matthias Schickinger, Martin Zacharias, and Hendrik Dietz, which was first published July 23, 2018; 10.1073/pnas.1800585115 (*Proc Natl Acad Sci USA* 115:E7512–E7521).

The authors note that, due to a printer's error, some of the text in the main article appeared incorrectly. On page E7518, right column, first full paragraph, line 7, "$\Delta_{seq} = 1$" should instead appear as "$\delta_{seq} = 1$."

The authors also note that Table S4 in the *SI Appendix* appeared incorrectly. The *SI Appendix* has been corrected online.

Published online September 17, 2018.

www.pnas.org/cgi/doi/10.1073/pnas.1814449115